Synergistic Deformation Mechanisms with Austenite, Ferrite and κ-Carbide During Flow Behavior in a Ferrite-Based Lightweight Steel

WENTING ZHU, SHUANGJIE CHU, and BO MAO

The high-temperature flow characteristics and dynamic microstructural evolution of a Fe−3.3Mn–9.6Al–0.3C ferritic-based duplex lightweight steel containing δ-ferrite, austenite and κ-carbide were systematically examined at strain rates and temperatures in the range of 0.01-10 s^{-1} and 800-1100 °C, respectively. Correlation of true stress-strain curves, constitutive equations with a processing map in the present steel was investigated in-depth. The results show that the most favorable hot working domains were achieved within the conditions of 950-1100 °C/0.01-1 s^{-1}. These optimum domains were associated with distinct underlying mechanisms resulting from different microstructural responses. Among them, the lamellar structures comprising intra-granular κ-carbides and austenite exhibited an evident strain gradient with the adjacent δ-ferrite. This gradient resulted in less lattice restriction, thereby promoting strain hardening instead of dynamic recrystallization. At a strain rate of 1 s^{-1}, the formed inter-granular κ-carbides were increased, which facilitated dynamic recrystallization and acted as an obstruction at grain boundaries to hinder the dynamic recrystallization grain enlargement. At higher strain rates (> 1 s^{-1}) and lower temperature (< 950 °C) unstable domain, the inhomogeneity in microstructure size and crystallographic orientation served as an indication of deformation instability. Throughout the plastic deformation, the deformation mechanisms were determined by κ-carbide hardening, continuous dynamic recrystallization marked by the gradual misorientation development of subgrains towards high-angle boundaries, and discontinuous dynamic recrystallization observed at the interfaces between δ-ferrite and the lamellar structures.

https://doi.org/10.1007/s11661-024-07540-3

I. INTRODUCTION

WITH the continuous progression of national fuel consumption and emission standards, the demand for energy-efficient systems continues to grow. This drives the development of high strength lightweight steels as a novel frontier in the realm of transportation applications. Among these, ferrite-based lightweight steels with elements ranging between 3-10 wt pct of Al, 2-5 wt pct of Mn, and 0.05-0.5 wt pct of C have garnered significant research interest for their low cost, superior comprehensive mechanical properties, significant reduction in density, and desirable anti-corrosion ability. These properties make such alloys attractive for a variety of applications in the automotive, construction, and military industries.

Despite the fact that the addition of Al element could prominently reduce the density of steels, this metallurgical alloying strategy typically suffers from the formation of undesirable microstructure features, which pose significant challenges for their processing and applications. A high Al content may result in the formation of excessive δ-ferrite and κ-carbide.[1–3] Given the lack of phase transformation, δ-ferrite tends to exhibit large grain sizes, often reaching dimensions of approximately 1 mm. In cases of higher rolling temperatures or inadequate cooling rates, κ-carbides tend to precipitate at the grain boundaries of δ-ferrite. Furthermore, κ-carbides within the δ-ferrite grains display a semi-coherent crystallographic relationship with respect to the δ-ferrite matrix, exhibiting a morphology characterized by coarse and elongated rod-like structures.[4] This is detrimental to both the plasticity and processing capabilities of high strength lightweight steels. Therefore, it is of critical importance to utilize thermomechanical

---

WENTING ZHU and BO MAO are with the School of Materials Science and Engineering, Shanghai Jiao Tong University, Shanghai 200240, P.R. China. Contact e-mail: bmao@sjtu.edu.cn SHUANGJIE CHU is with the School of Materials Science and Engineering, Shanghai Jiao Tong University and also with the Baoshan Iron & Steel Cooperation Limited, Shanghai 201900, P.R. China. Contact e-mail: sjchu@baosteel.com

Manuscript submitted January 16, 2024; accepted July 25, 2024.

processing-based approaches to control and tailor their microstructure.

Understanding the flow behavior and microstructure evolution of lightweight steels during hot working plays a critical role for the thermomechanical processing design and microstructure optimization. For lightweight steels containing solely δ-ferrite, Xu *et al.*[5] optimized the hot deformation parameters and found that higher strain rates and deformation temperatures facilitate the occurrence of discontinuous dynamic recrystallization behavior. Recrystallization stands out as the most effective approach for grain refinement to enhance the mechanical properties of steel.[6] However, for ferrite-based lightweight steels, the difference lies in the fact that the coexistence of austenite and δ-ferrite can result in distinct strain partitioning and load transfer, even in the initial stages of deformation. In addition, previous investigations have uncovered a noteworthy phenomenon wherein strain is transmitted from the softer ferrite phase to the harder austenite phase during subsequent deformation stages.[7,8] This phenomenon primarily arises from the differing deformation responses of these two phases and the non-uniform deformation occurring at the interphase boundaries.[9] More importantly, upon reaching a critical threshold of κ-carbide content, a notable alteration in the cooperative deformation behavior among the various phases within the microstructure is triggered. On account of different formation mechanisms, κ-carbide can be categorized into two distinct types: fine-layered intra-granular κ-carbide[10] and nano-dispersed inter-granular κ-carbide.[11] Both types of κ-carbides play significant roles in strengthening the steel by obstructing dislocation movement.[12,13] However, inter-granular κ-carbides, located at grain boundaries and comparatively larger in size, have the potential to cause embrittlement in the steel, as confirmed by Park *et al.*[14] In addition, Haase *et al.*[15] found that the interaction between intra-granular κ-carbides and dislocations results in the softening of the corresponding glide plane. From this perspective, it becomes apparent that the formation mechanisms underlying these two precipitate types, as well as their respective impacts on the ultimate properties of the steel, seem to exhibit considerable distinctions. Hence, it is imperative to undertake a comprehensive analysis of the dynamic precipitation behavior of κ-carbides and their synergistic deformation mechanisms with austenite and ferrite.

The current study aims to conduct a comprehensive investigation into the dynamic softening behavior and hot deformation mechanisms of a ferritic-based duplex lightweight steel. Constitutive equations and processing maps were established according to true stress-strain curves. Besides, the flow behaviors, microstructural evolution and various underlying mechanisms (such as dynamic recrystallization and dynamic precipitation) among multiple phases within both the "safe" and "unsafe" zones obtained from the processing map were elucidated in detail. The results of this study are poised to yield both fundamental significance and practical applications on the hot working of ferritic-based duplex lightweight steel for extensive utilization across industrial and transportation applications.

II. EXPERIMENTS

The lightweight steel, with a chemical composition of Fe−3.3Mn–9.6Al–0.3C (wt pct), was produced using the vacuum induction melting technique. The calculated density of this steel was approximately 6.86 g cm^{-3}. Compression specimens were cut from the ingot and processed to cylindrical dimension of 12 mm in length and 8 mm in diameter, ensuring that the upper and lower surfaces of compression specimens were vertically parallel. All specimens were degreased in an ultrasonic cleaner using ethanol. Hot compression experiments were performed using the Gleeble-3800 thermal simulation machine. A schematic representation of these experiments is depicted in Figure 1(a). The maximum true strain was 0.8 (corresponding to a maximum compression of 55 pct) at deformation temperatures of 800-1100 °C and strain rates of 0.01-10 s^{-1}. The specimen was heated to 1200 °C at a rate of 5 °C/s and held at this temperature for 3 min. Subsequently, the specimens were cooled to the deformation temperature at a rate of 5 °C/s and held for 30 s before compression to eliminate the temperature gradient within the specimen. After compression, the deformed specimens were quenched rapidly to retain the high-temperature microstructure.

Figure 1(b) shows the plane of dissection and area of interest for the following microstructure observation. The specimens were mechanically polished and etched in a 4 vol pct nital solution. Microstructural examinations were observed using an optical microscope (OM, BX53M) and a scanning electron microscope (SEM, NOVA NanoSEM) equipped with electron backscatter diffraction (EBSD). The EBSD scan was performed with a step size of 0.2 μm, and the resulting data were analyzed by orientation imaging microscopy (OIM) analysis software. Specimens for EBSD analysis were mechanically polished and then electropolished in a solution comprising 92 vol pct ethyl alcohol and 8 vol pct perchloric acid. The evolution of microstructure at some specific deformation conditions was further investigated through the application of a transmission electron microscope (TEM, JEM-2100F, operating at 200 kV). Thin foils with 3 mm diameter for TEM experiments were prepared by twin-jet electropolishing in a solution of 10 vol pct perchloric acid and 90 vol pct ethyl alcohol at − 20 ºC using a voltage of 23 V. X-ray diffraction (XRD) measurements of the as-cast steel were conducted by a D8 DaVinci X-ray diffractometer equipped with a CuKα target. The instrument operated at a current of 40 mA and a voltage of 40 kV, with a scan range of 40 to 120 deg and a scan speed of 2 deg/min.

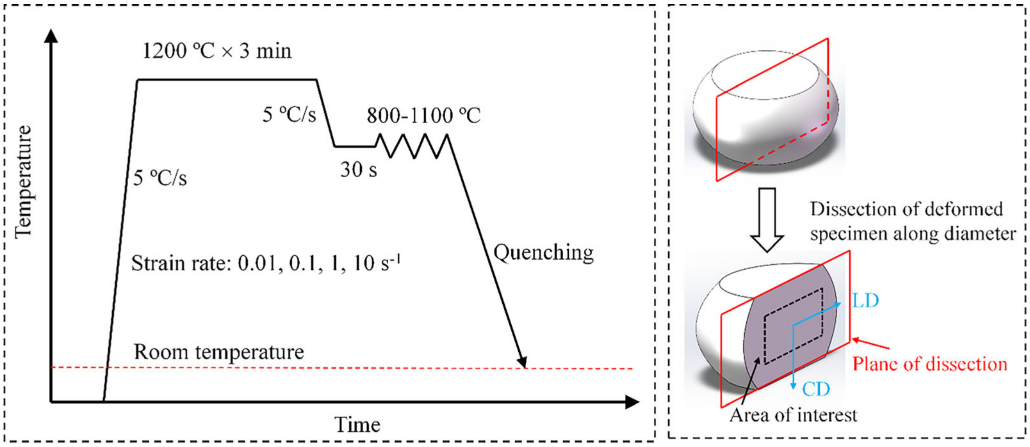

(a) (b)

Fig. 1—Schematic illustration of single-pass hot compression experiment (*a*) and the plane of dissection and area of interest for microstructure observation (*b*). CD is the compression direction, LD is the perpendicular to compression direction.

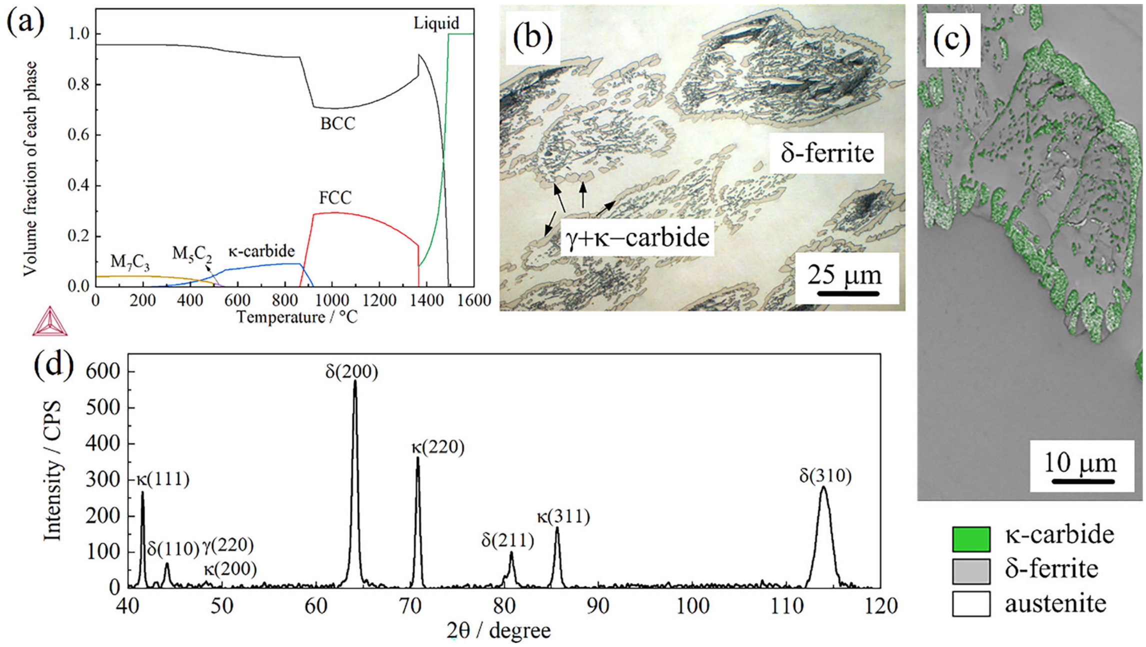

Fig. 2—(*a*) Equilibrium phase evolution of the steel in this study calculated from Thermo-Calc software. Initial microstructure of as-cast steel sample: (*b*) OM image, (*c*) phase map, and (*d*) XRD spectra. (*δ*: *δ*-ferrite, *γ*: austenite, and *κ*: kappa carbides).

III. RESULTS

A. *Microstructure Features of As-Cast Steel*

Figure 2(a) illustrates the variation in the equilibrium volume fraction of each phase with respect to temperature in the lightweight steel, as determined using the TCFE8.5 database in Thermo-Calc software. It can be found that the alloy initially solidifies as bcc *δ*-ferrite until most of the liquid is consumed. The remaining high-carbon liquid gradually transforms into fcc austenite. During subsequent air cooling, the fcc austenite continues to grow by consuming the bcc *δ*-ferrite. When the volume fraction of bcc *δ*-ferrite reaches its minimum value (~70.6 pct), the fcc austenite begins to transform into bcc α-ferrite and *κ*-carbide. Both *δ*-ferrite and α-ferrite possess the same crystal structure, distinguished primarily by whether they result from liquid-phase solidification or from the solid-phase transformation of austenite. Given that the content of α-ferrite is much lower than that of *δ*-ferrite, ferrite in this paper is collectively referred to as *δ*-ferrite.

From the representative OM image of the as-cast steel (Figure 2(b)), a multiphase microstructure consisting of *δ*-ferrite, austenite and *κ*-carbide was obtained as expected. To conduct a more detailed microstructural examination, EBSD was utilized to analyze the microstructure distribution of the as-cast steel, as illustrated in Figure 2(c). The phase map revealed that

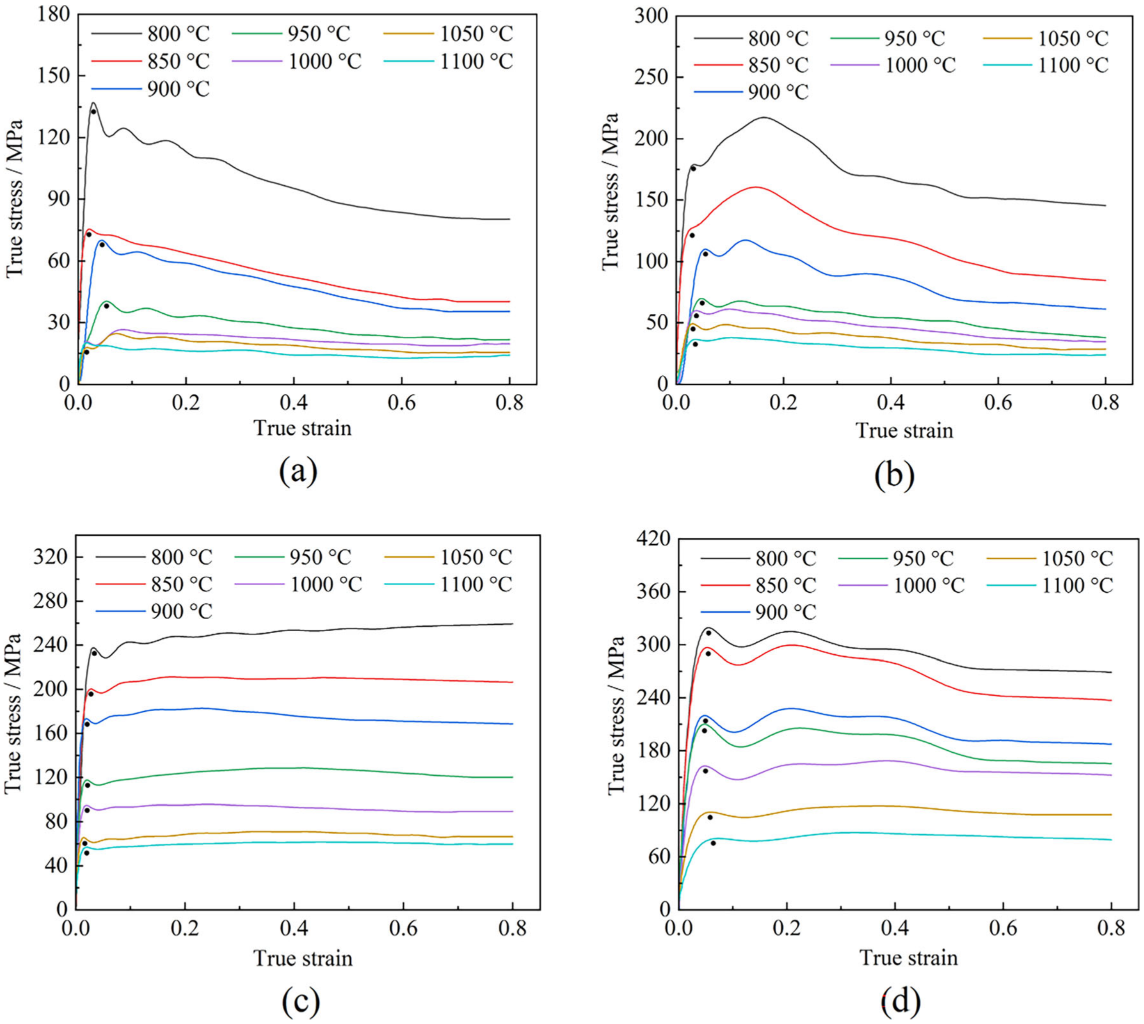

Fig. 3—Flow curves of ferritic-based lightweight steel within the deformation temperature range of 800-1100 °C at different strain rates: (*a*) 0.01 s^{-1}, (*b*) 0.1 s^{-1}, (*c*) 1 s^{-1}, (*d*) 10 s^{-1} (black dots representing the yield point-like phenomenon effect).

the fcc austenite exhibited a ring-like structure, with both its edge and interior covered with homogeneous κ-carbide. These phases were further verified by X-ray diffraction analysis, which identified distinct peaks corresponding to ferrite, austenite, and κ-carbide (Figure 2(d)). The volume fraction of retained austenite was quantitatively determined to be approximately 2.5 pct, which closely aligned with the 3.3 pct content obtained from the phase map.

B. *Flow Behavior*

Figure 3 shows the flow curves for this ferritic-based low-density steel. As plastic strain increased, the flow stress exhibited rapid growth, maintaining a wide peak before descending into a steady-state regime. The rise in flow stress can be attributed to the intense deformation resulting from dislocation generation and multiplication. Beyond the peak flow stress, a decline was observed at different strain rates and temperatures. This decline was attributed to the softening phenomenon caused by interactions between various mechanisms, such as dynamic recrystallization and the formation of an unstable microstructure post-deformation.

Focusing on the trends in flow curves at the onset of plastic deformation, there is a notable rise in the true stress-strain curves, followed by a sudden decline. This implied that a yield point-like phenomenon manifested itself in the work-hardening stage. Similar characteristics in flow curve configuration have been observed in other ferritic-based steels.[16,17] Unlike other ferritic-based steels where the yield point-like phenomenon was observed only at specific strain rates, the present steel exhibited this unusual behavior across all tested strain rates. Moreover, multiple peaks and valleys appeared on the flow curves at all four strain rates when the strain was below 0.6, as depicted in Figure 3. This behavior may be attributed to the synergistic effects of the multiphase microstructure, which contains δ-ferrite along with small amounts of austenite and κ-carbides.

C. *Constitutive Equation*

As mentioned earlier, the flow stress during plastic deformation at elevated temperatures is strongly affected by chemical composition, strain rate and temperature. The relationship among these factors satisfies the Arrhenius equation:

$$\dot{\varepsilon} = Af(\sigma)\exp\left(-\frac{Q}{RT}\right) \quad [1]$$

where A, Q, $\dot{\varepsilon}$, T and R refer to the material constant, the activation energy of deformation in kJ/mol, the strain rate in s^{-1}, deformation temperature in K, and the universal gas constant in J mol^{-1} K^{-1}, respectively. Additionally, $f(\sigma)$ represents the function related to flow stress. It can be described by a power law for low stresses when $\alpha\sigma < 0.8$[18] and an exponential law for high stresses when $\alpha\sigma > 1.2$,[18] while hyperbolic sine law has been confirmed to be valid across a wide range of stresses.[19]

$$f(\sigma) = \begin{cases} \sigma^{n_1} \\ \exp(n_2\sigma) \\ [\sinh(\alpha\sigma)]^n \end{cases} \quad [2]$$

Here, n_1, n_2, n and α are all material constants independent of temperature, where α is approximately the ratio of n_2 and n_1. Upon substituting Eq. [2] into Eq. [1] and subsequently applying logarithms to both sides, Eq. [1] can be expressed as:

$$\ln\dot{\varepsilon} = \ln A_1 + n_1 \ln\sigma \quad [3]$$

$$\ln\dot{\varepsilon} = \ln A_2 + n_2\sigma \quad [4]$$

$$\ln\dot{\varepsilon} = \ln A + n\ln\sinh(\alpha\sigma) - \frac{Q}{RT} \quad [5]$$

where A_1, A_2 and A are the material constants. Critical stress, steady stress, and peak stress are well-established characteristic stresses used in formulating constitutive equations. Considering their easier determination from the flow curves and greater relevance to industrial production, the peak stress, σ_P, is selected for calculation in this paper.[20]

The values of n_1 and n_2 can be derived from the slopes $n_1 = \left[\frac{\partial\ln\dot{\varepsilon}}{\partial\ln\sigma_P}\right]_T$ and $n_2 = \left[\frac{\partial\ln\dot{\varepsilon}}{\partial\sigma_P}\right]_T$ of Eqs. [3] and [4] (Figures 4(a) and (b)), respectively, and thus the value of α is calculated as ~ 0.011.

Given the premise of constant values for T and $\dot{\varepsilon}$, we can express Eq. [5] in an alternative form as:

$$n = \left[\frac{\partial\ln\dot{\varepsilon}}{\partial\ln[\sinh(\alpha\sigma_P)]}\right]_T \quad [6]$$

$$Q = 1000Rn\left[\frac{\partial\ln[\sinh(\alpha\sigma_P)]}{\partial\frac{1000}{T}}\right]_{\dot{\varepsilon}} \quad [7]$$

From Eqs. [6] and [7], the values of n and Q can be determined by evaluating the average slope of ln $\dot{\varepsilon}$ – ln[sinh($\alpha\sigma_P$)] and ln[sinh($\alpha\sigma_P$)]– 1000/T, as illustrated in Figures 5(a) and (b). The activation energy (Q) for thermal deformation is believed to be a vital physical parameter that provides insights into the rate-controlling deformation mechanism. The Q value exhibited a decreasing trend with decreasing strain rate. At higher strain rates (≥1 s^{-1}), Q consistently registered at a relatively high level, ranging between 350 and 370 kJ mol^{-1}. As the strain rate reduced to below 0.1 s^{-1}, Q fluctuated between 300-340 kJ mol^{-1}. Comparatively, the activation energy of a Fe–4Al–1.1Ni steel (277.2 kJ mol^{-1}) with a single δ-ferrite microstructure was lower than that of this duplex lightweight steel.[21] This difference can be ascribed to dynamic recrystallization of δ-ferrite absorbing a portion of the deformation energy.[22] Moreover, in the study on a Fe–11Mn–10Al–0.9C ferritic steel,[9] specimens containing κ-carbides were found to possess an activation energy approximately twice that of specimens without κ-carbides. This finding also explains the reason why the activation energy of the high Al lightweight steel containing δ-ferrite with a small amount of austenite in Reference[23] (272.08 kJ mol^{-1}) was lower than that of the present steel. During thermal deformation, a higher Q value resulted in the enhanced blocking effects of dislocation motion, especially in the interaction with other dislocations, precipitates, grain boundaries.[24] However, relying solely on a deformation activation energy map may not provide definitive guidelines for determining the optimal processing regime for the studied steel. To draw more robust and reliable conclusions, subsequent results included an in-depth exploration of the processing map and meticulous analysis of microstructures.

D. *Processing Map*

Based on the dynamic materials model proposed by Prasad,[25] the correlation between strain rate and flow stress can be expressed by the following constitutive equation:

$$\sigma = K\dot{\varepsilon}^m \quad [8]$$

where m refers to the strain rate sensitive index, and K to a material constant. Taking the logarithm on both sides of Eq. [8], the expression for m becomes:

$$m = \frac{\partial\ln\sigma}{\partial\ln\dot{\varepsilon}} \quad [9]$$

Furthermore, the value of m serves as an indicator of the partitioning of the total dissipated power P in the process of plastic deformation. This total dissipated power comprises two components: one due to temperature rise (G) and the other resulting from microstructural evolution (J). The mathematical expression is expressed as:

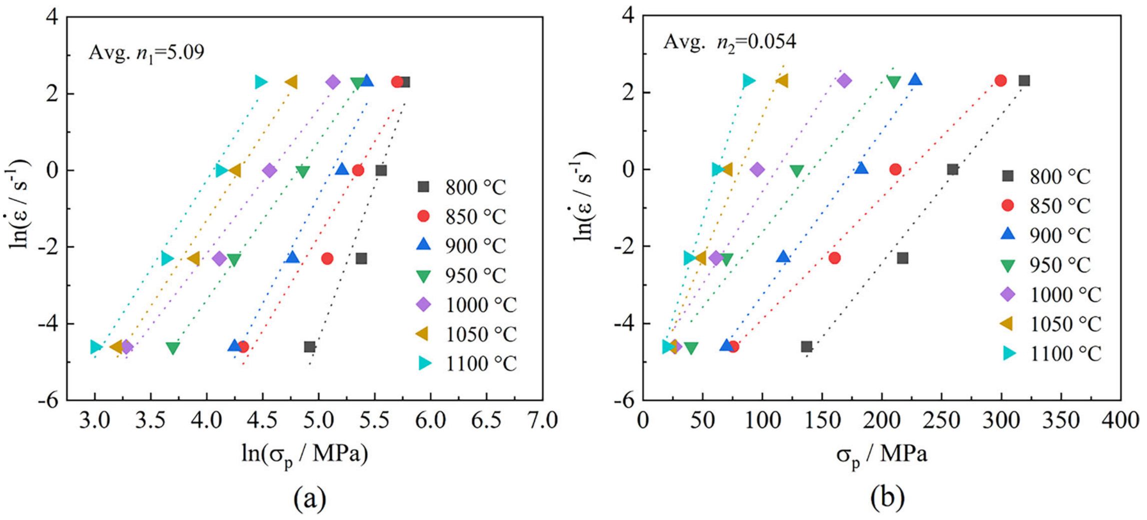

(a) (b)

Fig. 4—Liner relationship of (*a*) $\ln \dot{\varepsilon} - \ln \sigma_P$ and (*b*) $\ln \dot{\varepsilon} - \sigma_P$.

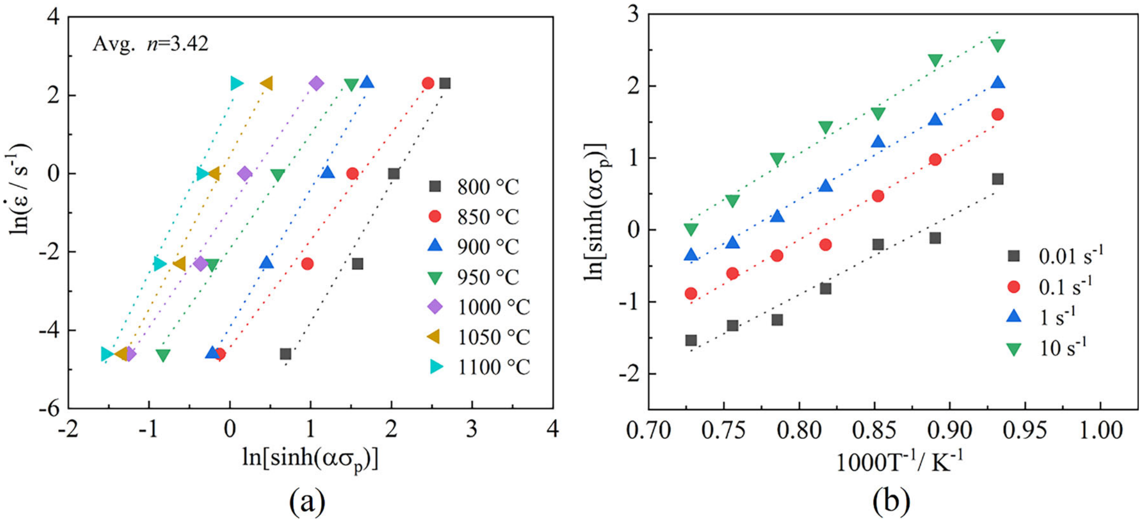

(a) (b)

Fig. 5—Liner relationship of (*a*) $\ln \dot{\varepsilon} - \ln[\sinh(\alpha\sigma_P)]$ and (*b*) $\ln[\sinh(\alpha\sigma_P)] - 1000/T$.

$$P = \sigma\dot{\varepsilon} = G + J = \int_0^{\sigma} \dot{\varepsilon}\, d\sigma + \int_0^{\dot{\varepsilon}} \sigma\, d\dot{\varepsilon} \qquad [10]$$

It can be deduced that the power partitioning between *J* and *G* is determined by the flow stress behavior of the steel, denoted by *m* in Eq. [11]:

$$\frac{\partial J}{\partial G} = \frac{\sigma d\dot{\varepsilon}}{\dot{\varepsilon} d\sigma} = \frac{\partial \ln \sigma}{\partial \ln \dot{\varepsilon}} = m \qquad [11]$$

The relationship between $\ln \sigma$ and $\ln \dot{\varepsilon}$ lends itself to a well-fitted cubic polynomial:

$$\ln \sigma = a + b \ln \dot{\varepsilon} + c(ln\dot{\varepsilon})^2 + d(ln\dot{\varepsilon})^3 \qquad [12]$$

By solving the first derivation of $\ln \sigma$ to $\ln \dot{\varepsilon}$ in Eq. [12], the value of *m* can be obtained as follows:

$$m = \frac{\partial \ln \sigma}{\partial \ln \dot{\varepsilon}} = b + 2c(ln\dot{\varepsilon}) + 3d(ln\dot{\varepsilon})^2 \qquad [13]$$

To quantify the energy proportion energy expended on microstructural evolution, Prasad *et al.*[25] defined the power dissipated factor (η) to represent the relationship between power dissipation characteristics and microstructure:

$$\eta(T, \dot{\varepsilon}) = \frac{J}{J_{\max}} = \frac{2m}{m+1}\bigg|_{\varepsilon} \qquad [14]$$

Plotting the calculated η values against temperature and strain rate results in the power dissipation map, which is commonly presented in the form of two-dimensional contour map illustrating iso-efficiency. During deformation, domains where the greater value η is located correspond to microstructural mechanisms that effectively consume energy. These domains are considered capable of optimizing deformation conditions through meticulous microstructure control and reproducibility. However, in high-efficiency domains, the instability of deformation caused by various forms of damage may deteriorate the processing performance of materials. Thus, introducing an instability criterion becomes essential to enhance the accuracy of processing map predictions. Combining the dynamic materials model with the plastic flow theory proposed by Ziegler,[26] the instability criterion under a given deformation condition is expressed as a dimensionless parameter, $\xi(\dot{\varepsilon}, T)$, based on the principle of maximum entropy production rate:

$$\xi(\dot{\varepsilon}, T) = \frac{\partial \ln\left(\frac{m}{m+1}\right)}{\partial \ln \dot{\varepsilon}} + m < 0 \qquad [15]$$

Therefore, in the temperature-strain rate spatial domain, the two-dimensional contour map depicting the variation of $\xi(\dot{\varepsilon})$ is referred to as the instability map. For a constant strain condition, the processing map can be plotted by superimposing the two-dimensional contour maps of ξ and η. Figure 6 shows the hot processing map of this lightweight steel at a true strain of 0.8, where the green domain (Domain I), white domain (Domain II) and grey domain (Domain III) correspond to the safe deformation domain with an efficiency range of 40-50 pct, safe deformation domain with an efficiency range of 30-40 pct and unsafe domain, respectively.

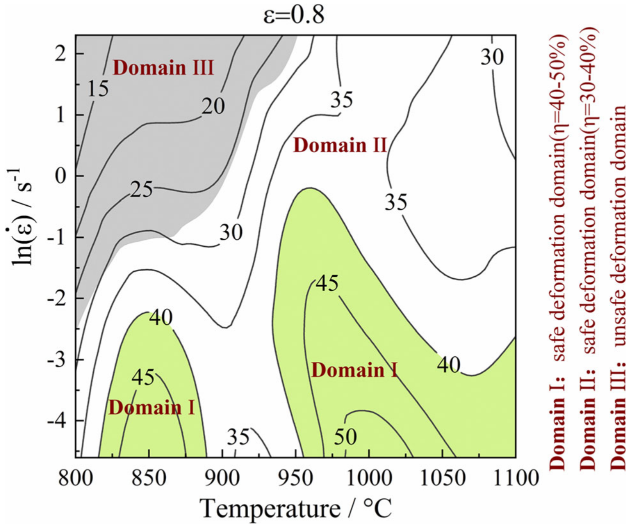

Fig. 6—Hot processing map of ferritic-based lightweight steel at strain of 0.8. The green domain, white domain and grey domain correspond to the safe domains with efficiency range of 40-50 and 30-40 pct, and unsafe domain, respectively (Color figure online).

E. *Microstructural Evolution*

The dynamic response of the microstructure in duplex lightweight steel has garnered significant attention owing to the complex and synergistic deformation behavior exhibited by its constituents, namely ferrite, austenite, and κ-carbide. Consequently, there is a compelling need for a comprehensive analysis to explore and understand the microstructural evolution occurring during deformation in each of the six specimens selected from the three representative domains below.

Domain I represents a "safe domain" within the deformation process, characterized by an efficiency range of 40-50 pct under conditions of 950-1100 ºC/800-900 ºC and 0.01-0.1 s^{-1}. EBSD images of the specimen associated with the maximum η of 50 pct were observed within this parameter range, as depicted in Figure 7. The average grain size in the LD direction of δ-ferrite was determined to be approximately 86 ± 12 μm. The grain orientation spread (GOS) map for grains exhibiting GOS values of 0-2 deg indicated that ~ 35.9 pct of the grains underwent recrystallization in the microstructure (Figure 7(a)). This finding was inconsistent with the calculated maximum efficiency result, as GOS values for all the remaining grains lied within the interval of 2 to 6 deg. This contradiction can be attributed to the occurrence of the eutectoid reaction in the austenite, resulting in the newly formed κ-carbide and ferrite. The phase map reveals that both product phases grew into lamellar structures, as shown in Figure 7(b). Notably, δ-ferrite in the recovery stage surrounding these lamellar structures exhibited significant angular deviation, as evident from the grain reference orientation deviation (GROD) map in

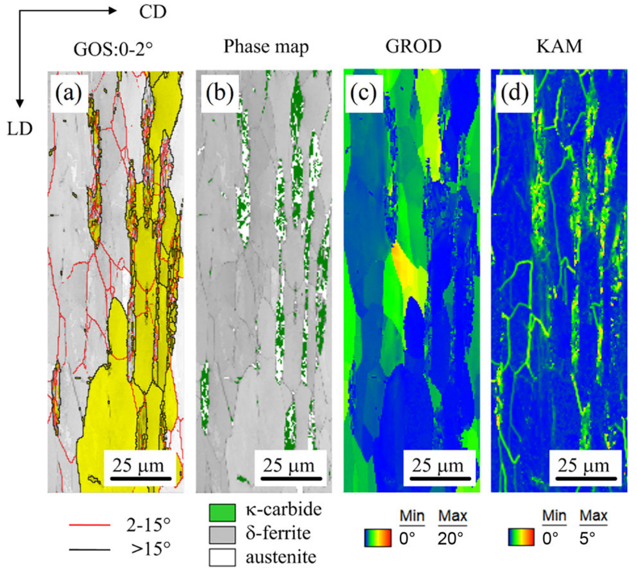

Fig. 7—EBSD analysis of ferritic-based lightweight steel deformed at a temperature of 1000 ºC and strain rate of 0.01 s^{-1}: (*a*) GOS map of the grains with GOS values of 0-2 deg overlying low-angle grain boundaries (LAGBs) and high-angle grain boundaries (HAGBs) represented by red and black lines, respectively (yellow color represents recrystallized region), (*b*) phase map (green color, grey color, and white color represent κ-carbide, δ-ferrite and austenite, respectively); (*c*) GROD map; (*d*) KAM map (Color figure online).

Figure 7(c). In particular, the angular deviation related to the deformed δ-ferrite grains was most prominent at the interfaces of the recovery and recrystallization. Limitations on lattice rotation imposed additional hardening effects on the δ-ferrite grains adjacent to the lamellar structures. Furthermore, Figure 7(d) presents the kernel average misorientation (KAM) map, providing a qualitative depiction of the local strain distribution.[27] This map shows higher values within the lamellar structures and their vicinity. The local strain distribution inside δ-ferrite grains was influenced by their proximity to these lamellar structures, resulting in distinct strain levels. Specifically, there was a relatively lower strain between the interior of grains and higher local strain located in the regions adjacent to lamellar structures. As a result, the division of δ-ferrite grains into distinct regions with varying work-hardening levels occurred due to the strain gradient and lattice rotation. In other words, these regions underwent strain hardening rather than recrystallization.

Figure 8 shows another safe domain with an efficiency range of 40-50 pct. When the specimen deformed at 850 ºC/0.01 s^{-1}, the volume fraction of austenite was nearly 0, primarily due to the transformation of most austenite into dispersed intra-granular carbides (Figure 8(a)). As shown in the GOS map (Figure 8(b)), the recrystallized grains were measured to be 64 pct. Fine recrystallized grains nucleated at the grain boundaries of non-recrystallized large grains and intragranular carbides. As compression progressed, non-recrystallized grains underwent deformation on one side while forming dislocations at the grain boundaries on the other side (Figure 8(c)), leading to continuous formation of new recrystallized grains within the grains. The combined effects of dynamic softening and κ-carbide hardening inhibited the formation of voids and cracks.

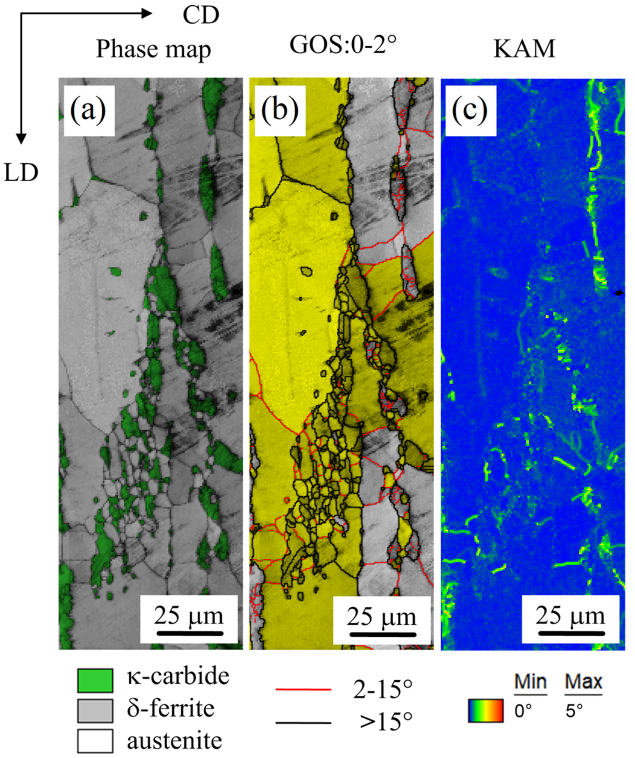

Fig. 8—EBSD analysis of ferritic-based lightweight steel deformed at 850 ºC/0.01 s^{-1}. (*a*) Phase map; (*b*) GOS map of the grains with GOS values having 0-2 deg; (*c*) KAM map. (The legend color code of recrystallized region, boundary and phase can be referred to Fig. 7).

Domain II represents the safe zone with a power efficiency of 35-40 pct as thermal deformation proceeds, occurring at 900-950 ºC/0.01-0.1 s^{-1} and 950-1100 deg/1-10 s^{-1}, respectively. Figures 9(a) through (d) display the EBSD maps of the specimen deformed at 1000 ºC/1 s^{-1} (η = 35 pct). Analysis of the GOS map reveals that the recrystallization fraction in this specimen reached 92.4 pct, with only 7.6 pct of grains in the recovery stage (GOS values of 2-6 deg) (Figure 9(a)). The recrystallized grains displayed an equiaxed morphology and had grown to an average size of 43 ± 10 μm. As the strain rate increased, leading to a reduction in grain size, there was a corresponding decrease in power efficiency.[28] The degree of recrystallization in the specimen subjected to deformation at 1000 ºC/1 s^{-1} significantly exceeded that observed in the specimen deformed at 1000 ºC/0.01 s^{-1}. This difference was attributed to the precipitation of κ-carbides along the grain boundaries of δ-ferrite (Figure 9(b)). The presence of these inter-granular κ-carbides acted as effective impediments to the growth of dynamically recrystallized grains, serving as pinning agents along the grain boundaries. The strong constraint exerted by the inter-granular κ-carbides on the δ-ferrite grains severely restricted their ability to rotate during plastic deformation (Figure 9(c)). Similarly, in the specimen subjected to 1000 ºC/1 s^{-1}, the δ-ferrite grains enclosed by inter-granular κ-carbides had the least KAM value (Figure 9(d)).

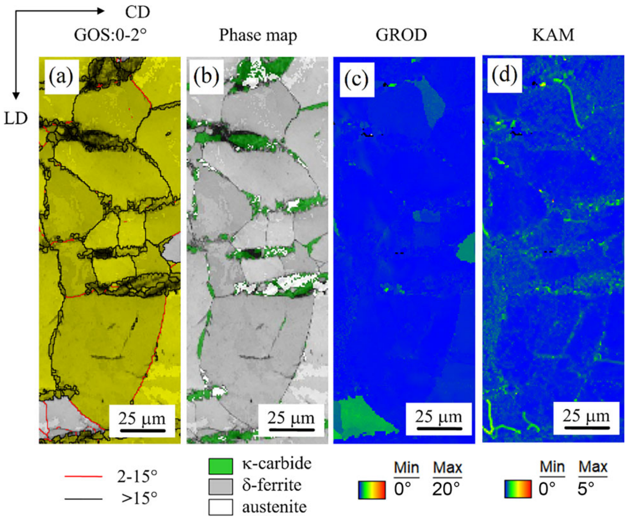

Fig. 9—EBSD analysis of ferritic-based lightweight steel deformed at 1000 ºC/1 s^{-1}. (*a*) GOS map of the grains with GOS values having 0-2 deg; (*b*) phase map; (*c*) GROD map; (*d*) KAM map. (The legend color code of recrystallized region, boundary and phase can be referred to Fig. 7).

Upon reaching a strain rate of 10 s^{-1}, the extent of recrystallization fraction dramatically decreased to 22.8 pct (Figure 10(a)). As indicated by the black arrows in Figure 10(a), localized recrystallization occurred within the δ-ferrite grains, where only a small number of recrystallized grains were enclosed by HAGBs. It is believed that these grains developed from subgrains with significant misorientation primarily located within the parent δ-ferrite grains, as depicted by the white rectangle in Fig 10(a). Additionally, notable lattice rotation is evident at the interfaces of HAGBs and LAGBs in the GROD map (Figure 10(c)). The white-colored arrows in Figures 10(a) and (c) denote these interfaces of HAGBs and LAGBs. This phenomenon signifies that the initial deformation of the δ-ferrite grains primarily occurred at these interfaces. By comparison (Figures 9(a) and 10(a)), it is evident that the relative frequency of LAGBs in the specimen deformed at 1000 ºC/1 s^{-1} (10 pct) was lower than that at 1000 ºC/10 s^{-1} (57.3 pct), indicating a diminished occurrence of dynamic recrystallization as the strain rate increased. This is attributed to insufficient time for Mn and C atoms to diffuse towards grain boundaries. Therefore, the formation of lamellar structures preceded the formation of κ-carbides at the grain boundaries, resulting in a lower extent of dynamic recrystallization.

Similar to the specimen deformed at 1000 ºC/1 s^{-1}, at a decreased temperature of 950 ºC, the microstructure at the same strain rate also exhibited a high recrystallization fraction of 81.7 pct as well (Figure 11(a)). Figure 11(c) presents the representative inverse pole figure (IPF) map for the specimen undergoing deformation at 950 ºC/1 s^{-1}. For the BCC phase, the IPF color code with its distinct color gradient vividly highlighted the variation in the orientation of the δ-ferrite grains. The results observed in the IPF map revealed that the δ-ferrite in this specimen deformed homogeneously.

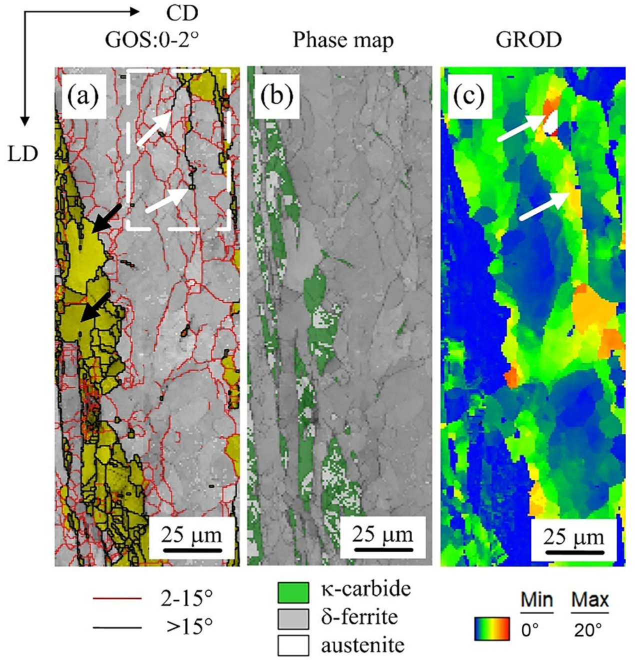

Fig. 10—EBSD maps of ferritic-based lightweight steel deformed at 1000 ºC/10 s^{-1}. (*a*) GOS map of the grains with GOS values having 0-2 deg; (*b*) phase map; (*c*) GROD map. (The legend color code of recrystallized region, boundary and phase can be referred to Fig. 7).

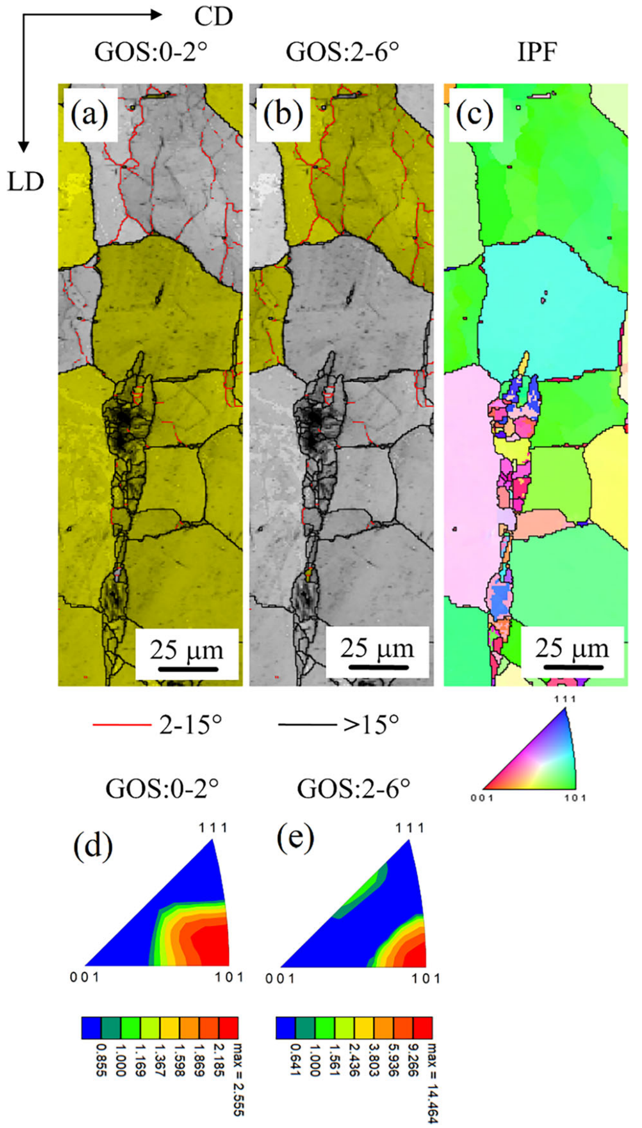

Fig. 11—EBSD maps of ferritic-based lightweight steel deformed at 950 ºC/1 s^{-1}. (*a*, *b*) GOS maps of grains with GOS values having 0-2 and 2-6 deg, respectively, and the (*d*, *e*) corresponding IPF maps of different GOS ranges; (*c*) IPF map. (The legend color code of recrystallized region, boundary and phase can be referred to Fig. 7).

Domain III is identified as an "unsafe domain" for thermal deformation, residing within the parameter range characterized by a strain rate of 0.1-10 s^{-1} and a temperature of 800-950 ºC. At 950 ºC/10 s^{-1}, the specimen exhibited that 33.1 pct of the grains possess GOS values below 2 deg, 56.2 pct of the grains had GOS values ranging from 2 to 6 deg, and the remaining grains fell within the range of 6-9 deg (Figures 12(a) through (c)). One of the vital factors contributing to the appearance of the "unsafe domain" during deformation was the crystallographic orientation of the

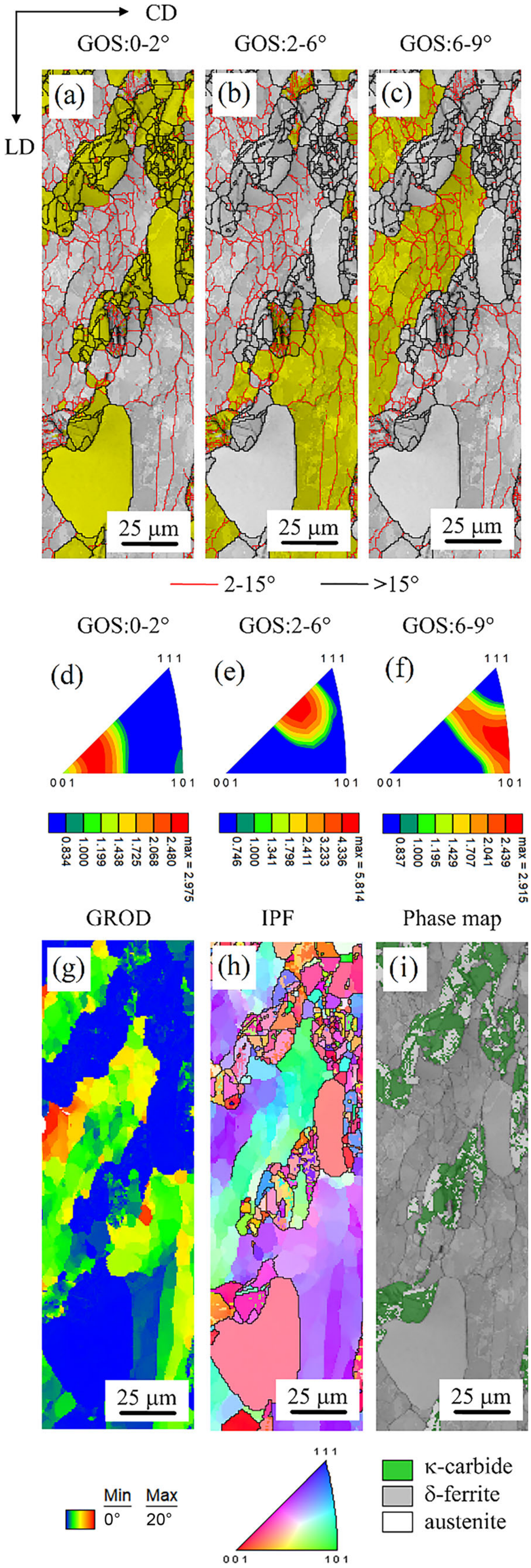

◀Fig. 12—EBSD maps of ferritic-based lightweight steel deformed at 950 ºC/10 s^{-1}. (*a* through *c*) GOS maps of grains with GOS values having 0-2, 2-6 and 6-9 deg, respectively, and the (*d* through *f*) corresponding IPF maps of different GOS ranges. (*g*) GROD map; (*h*) IPF map; (*i*) phase map. (The legend color code of recrystallized region, boundary and phase can be referred to Fig. 7).

microstructures. Consequently, a separate analysis is conducted to scrutinize the crystallographic orientation of δ-ferrite grains with diverse GOS values. Figures 12(d) through (f) illustrate IPF maps depicting δ-ferrite grains with varying GOS values at 950 ºC/10 s^{-1}. BCC phases with GOS values ranging from 0 to 2 deg were orientated along the < 001 > crystallographic direction. For GOS values within 2-6 deg, BCC phases predominantly aligned along the < 112 > crystallographic direction. In contrast, BCC phases with GOS values exceeding 6 deg exhibited a greater tendency to rotate towards the < 112 > , < 212 > and < 101 > crystallographic directions, leading to an augmented angular deviation in the GROD map, as depicted in Figure 12(g). For δ-ferrite grains deformed at 950 ºC/1 s^{-1}, the crystallographic orientation with GOS values spanning from 0-2 and 2-6 deg was indicated in Figures 11(d) and (e). It is noted that a significant number of grains in these GOS value ranges were oriented along the < 101 > crystallographic direction. This revealed an inhomogeneous distribution of crystallographic orientation in δ-ferrite grains at higher strain rates, consistent with the findings from the IPF map (Figure 12(h)). Such inhomogeneity in crystallographic orientation led to strain localization and concentration during plastic deformation, ultimately resulting in material instability.

When the deformation temperature decreased to 850 ºC, the specimen entered the unsafe region. The most likely contributing factor was the presence of an inhomogeneous microstructure resembling a necklace, characterized by fine equiaxed grains surrounding the coarse prior grains, as shown in the representative IPF map (denoted by the black rectangle in Figure 13(a)). The interfaces between these grains of varying sizes exhibited significant angular deviation (Figure 13(b)). Hence, the presence of a mixed crystal microstructure is unfavorable for achieving uniform deformation in the subsequent processing stages, and it can also result in flow instability due to localized deformation. The corresponding GOS map illustrated a significant proportion of dynamically recrystallized grains (~ 82.6 pct) in this deformed specimen (Figure 13(c)). Compared to the specimen deformed at 950 °C/10 s^{-1}, the higher proportion of recrystallized grains obtained in this specimen can be attributed to two main factors. Firstly, the temperature of 850 °C fell within the κ-carbide formation range, which favored the nucleation and growth of κ-carbides. Secondly, the high strain rate of 10 s^{-1} induced significant stored energy and adiabatic heating, both of which promoted the increased occurrence of κ-carbides either within the grains or at grain boundaries. As shown in Figure 13(d), a TEM image of

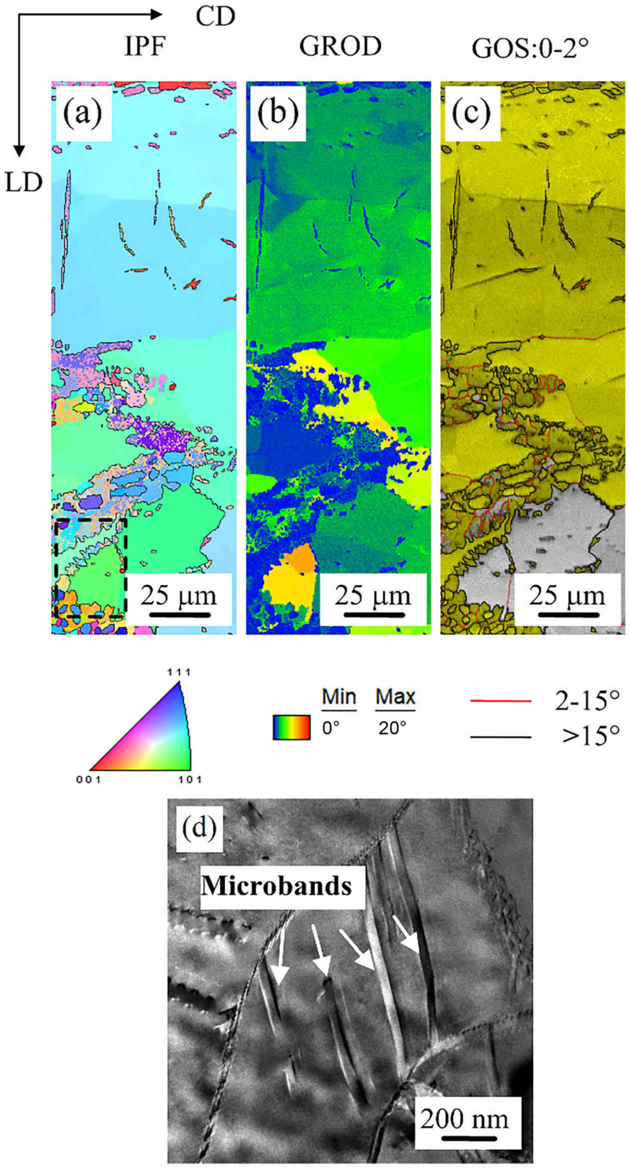

Fig. 13—EBSD maps of ferritic-based lightweight steel deformed at 850 ºC/10 s^{-1}. (*a*) IPF map; (*b*) GROD map; (*c*) GOS map of the grains with GOS values having 0-2 deg; (*d*) TEM image showing the micro-bands. (The legend color code of recrystallized region, boundary and phase can be referred to Fig. 7) (Color figure online).

the deformed δ-ferrite grains in the identical specimen highlighted the distinct presence of micro-bands.

IV. DISCUSSION

As reported by Momeni,[29] the kinetics of dynamic recrystallization comply with the following equation as strain increases based on the Johnson-Mehl-Avrami-Kolmogorov (JMAK) model:

$$F_X = 1 - \exp\left[-k\left(\frac{\varepsilon - \varepsilon_c}{\varepsilon_p}\right)^q\right], \qquad [16]$$

where F_X refers to the volume fraction of dynamic recrystallization, ε_p to the peak strain, ε_c to the critical strain at which dynamic recrystallization initiates,[30] k and q to the constant and Avrami exponent, respectively. The *q* value can be evaluated from the linearization of Eq. [16] at different deformation conditions as shown in Eq. [17].

$$q = \frac{\partial \ln\left(\ln \frac{1}{1-F_X}\right)}{\partial \ln \frac{\varepsilon - \varepsilon_c}{\varepsilon_p}} \qquad [17]$$

To determine the q value, the volume fraction of dynamic recrystallization is obtained by calculating grain orientation spreads lower than 2 deg in the GOS map. The corresponding graphic data for two typical deformation conditions are indicated in Figure 14, resulting in q values of 0.78 and 2.65, respectively.

For the discontinuous dynamic recrystallization mechanism ($q \approx$ 1-3) observed in other alloys,[31,32] the q value of the specimen deformed at 1000 °C/10 s^{-1} is much lower. This observation is consistent with the results reported in some other low-density steels.[33,34] It is ascribed to the synergistic effects of sluggish recrystallization kinetics, strong dynamic recovery,[35] and the inhomogeneous nucleation and growth of strain-free grains,[36] resulting in a lower q value. More importantly, this is also reflected in the wave-like flow curves at this strain rate. Considering that the presence of κ-carbide and strain partition in dual phases can make the mechanism of dynamic recrystallization for the specimen at 10 s^{-1} more complicated, it is essential to conduct an in-depth analysis of the deformation mechanisms.

Upon initiating deformation at 1000 °C/10 s^{-1}, the emergence of sub-boundaries within the δ-ferrite became distinctly observable (Figure 15(a)). Subsequently, as the strain increased to 0.4 and 0.6, a complex network of low and medium-angle grain boundaries developed within the ferrite grains, as depicted in Figures 15(b) and (c). Continuing the deformation process until a strain of 0.8 was reached, it was observed that certain sub-boundaries underwent a significant misorientation exceeding 15 deg. This transformation effect led to the formation of HAGBs (Figure 15(d)). The misorientation distribution plot corresponding to different strain levels revealed a continuous evolution in the microstructural characteristics of the δ-ferrite. There was a clear and progressive development of HAGBs when the strain was in the range of 0.2-0.8, as shown in Figure 16.

For the TEM image acquired at a strain of 0.2 (Figure 17(a)), the interior of deformed δ-ferrite grains was characterized by the substructures and cell walls with high dislocation densities. The dislocations became confined and absorbed by the pre-existing sub-boundaries that were generated during the early stage of deformation, resulting in an elevation in their misorientation (Figure 16). The white rectangle in Figure 15(a) shows the misorientation evolution from LAGBs, MAGBs to HAGBs due to dislocation rearrangement. This ultimately facilitated the development of substructures located within the δ-ferrite grains that were partially delimited by LAGBs and HAGBs (denoted as

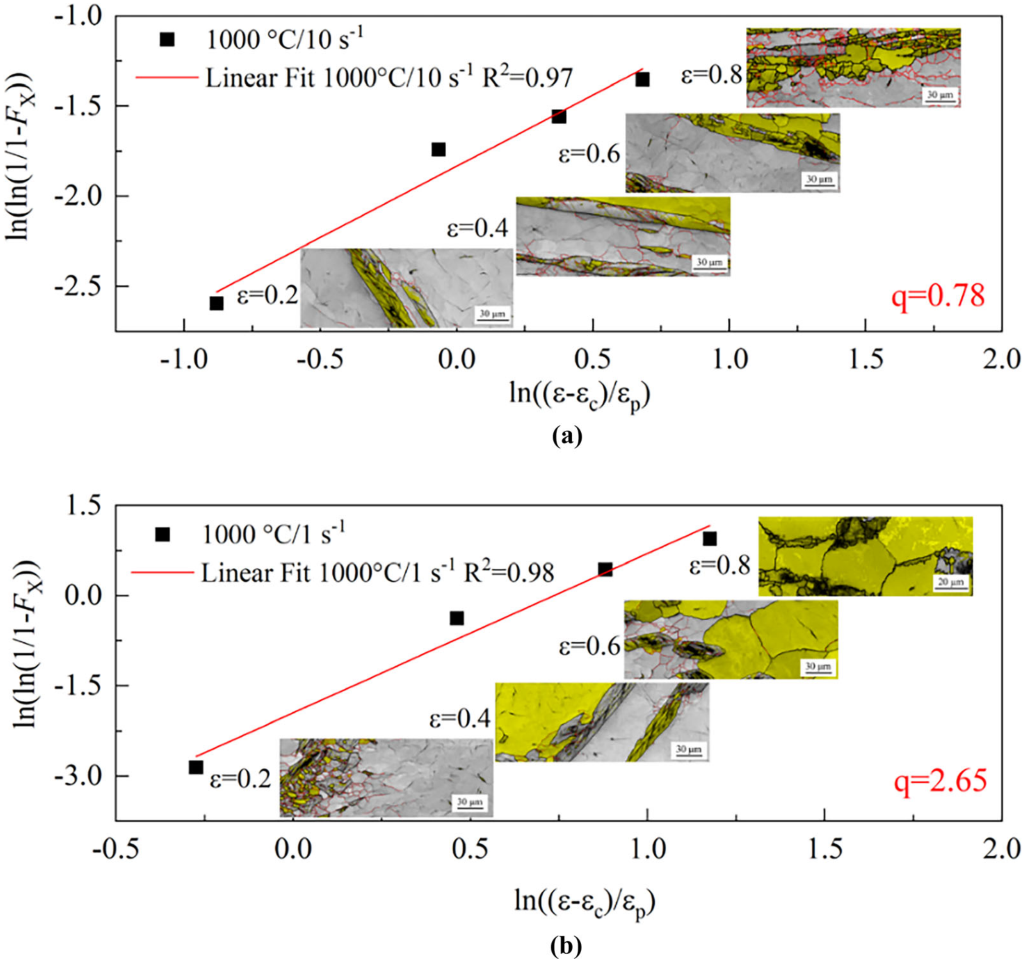

Fig. 14—Avrami graphs at 1000 °C/10 s^{-1} (*a*) and 1000 °C/1 s^{-1} (*b*) for the determination of q. The inset figures are corresponding GOS maps at different strains.

white arrows in Figures 15(b) through (d)). The mechanism responsible for the development of such substructures in the current duplex lightweight steel is commonly categorized as the 'extended dynamic recovery' mechanism or continuous dynamic recrystallization mechanism, which is documented to be prevalent in a variety of duplex lightweight steels. This finding aligned with the continuous dynamic recrystallization mechanism model in Reference,[37] indicating that LAGBs generated by dynamic recovery preferred to be transformed into HAGBs through the continual assimilation of dislocations in the process of continuous dynamic recrystallization (Figures 15, 16, and 17). However, some dynamic recrystallization grains bounded by the HAGBs are perceptible at a deformation of 1000 ºC/10 s^{-1} and at a strain of 0.8 (denoted by orange arrows in Figure 15(d)). Compared to the continuous dynamic recrystallization grains marked by white arrows, newly formed dynamic recrystallization grains are primarily located at the boundaries of δ-ferrite and the lamellar structures. As shown in Figure 17(b), a substantial number of linear dislocations are conspicuously evident within the interior of the δ-ferrite grains at a maximum strain of 0.8. This observation essentially implied that these newly formed grains underwent dynamic nucleation and experienced plastic deformation in the process of straining. As the strain continued to be applied, the increase in the values of the relative frequency of boundaries having a higher misorientation angle (>15 deg) and corresponding average misorientation value verified the nucleation and growth of newly formed grains during deformation at a high-temperature (Figure 16).

Note that some boundaries of dynamic recrystallization grains were characterized as bulging features, influenced by the variation in strain energy between adjacent grains, as shown in Figure 18(d) (denoted by yellow arrows). It can be observed from the KAM map that such boundaries exhibited curvature towards the high KAM region. This curvature suggested a deformation-driven migration of the boundaries towards the area experiencing significant strain. During the initial plastic deformation (at a strain of 0.2), the austenite phase underwent deformation first and accumulated a higher degree of strain, while the ferrite phase remained in the elastic stage resulted from the existence of hard κ-carbide particles. The KAM map confirmed that most strains were pronouncedly localized within the austenite

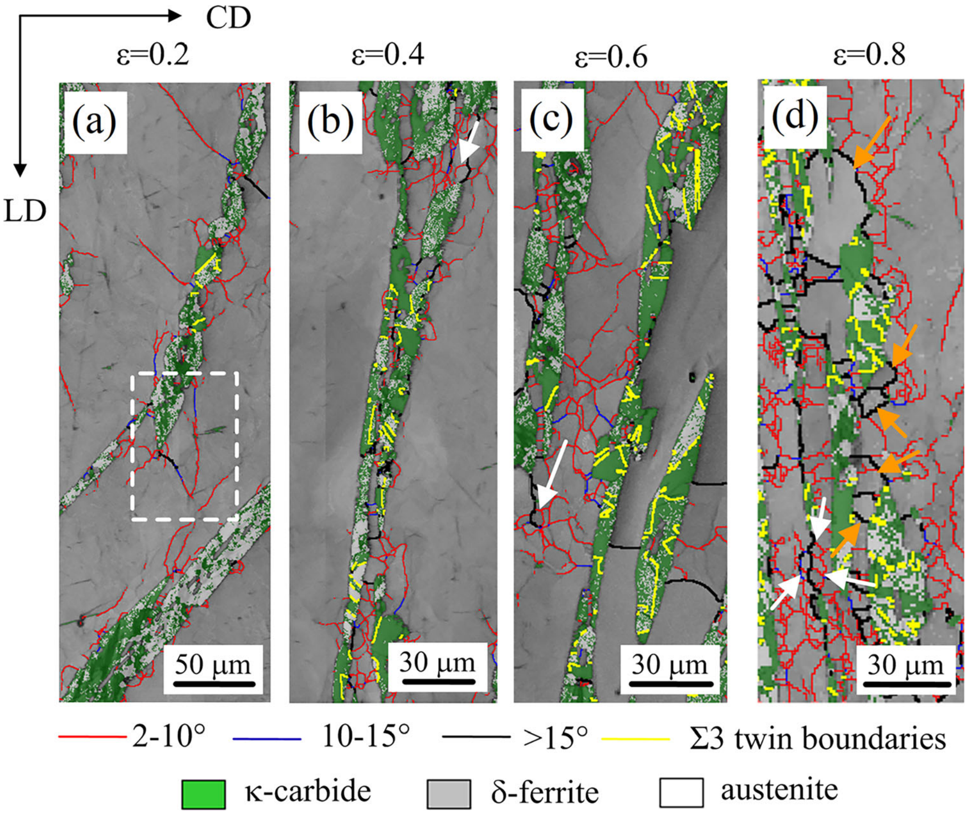

Fig. 15—Phase maps of ferritic-based lightweight steel under deformation conditions of 1000 ºC/10 s^{-1} at different strains: (*a*) 0.2; (*b*) 0.4; (*c*) 0.6; (*d*) 0.8.

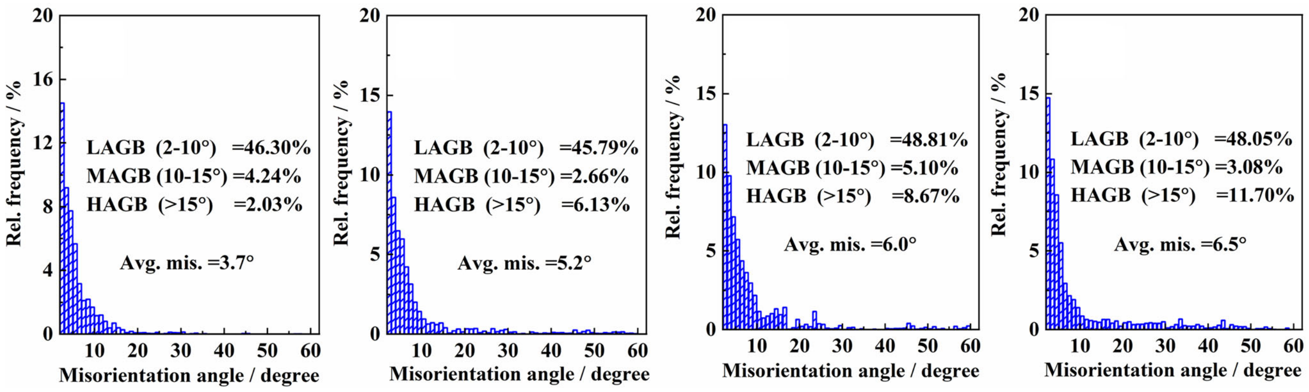

(a) (b) (c) (d)

Fig. 16—Relative frequency of different misorientation angles at 1000 ºC/10 s^{-1}: (*a*) 0.2; (*b*) 0.4; (*c*) 0.6; (*d*) 0.8.

phase, as indicated in Figure 18(a). Due to the limitation of the hard κ-carbide, the soft austenite is unable to deform without hindrance, leading to the development of a plastic strain gradient within the austenite adjacent to the phase interphase. As reported by Ashby,[38] the strain gradient may cause an increase in geometrically necessary dislocation density in the austenite, thus generating high back stress. This made an increase in the hardness of the soft austenite phase, which even equaled to δ-ferrite and κ-carbide. Accordingly, the load shifted from austenite to κ-carbide and δ-ferrite, ultimately resulting in the occurrence of the flow stress inflection point at all strains (denoted by black dots in Figure 3).

Moreover, a prominent presence of $\sum 3$ twin boundaries can be identified within the κ-carbides (indicated by yellow lines), as shown in Figure 15. The larger κ-carbides, with their inherent hardness, posed challenges for dislocation slip deformation. As slip became less favorable due to the obstruction by carbides, twinning emerges as a favored mode of plastic deformation. The formation of twin boundaries allowed the

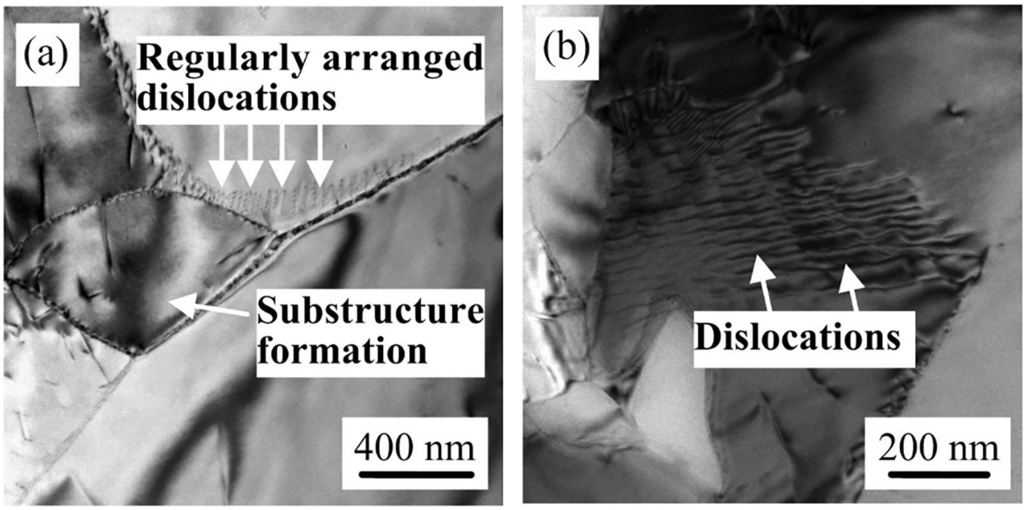

Fig. 17—TEM image of ferritic-based lightweight steel at a deformation of 1000 ºC/10 s^{-1} at different strains of (*a*) 0.2 and (*b*) 0.8.

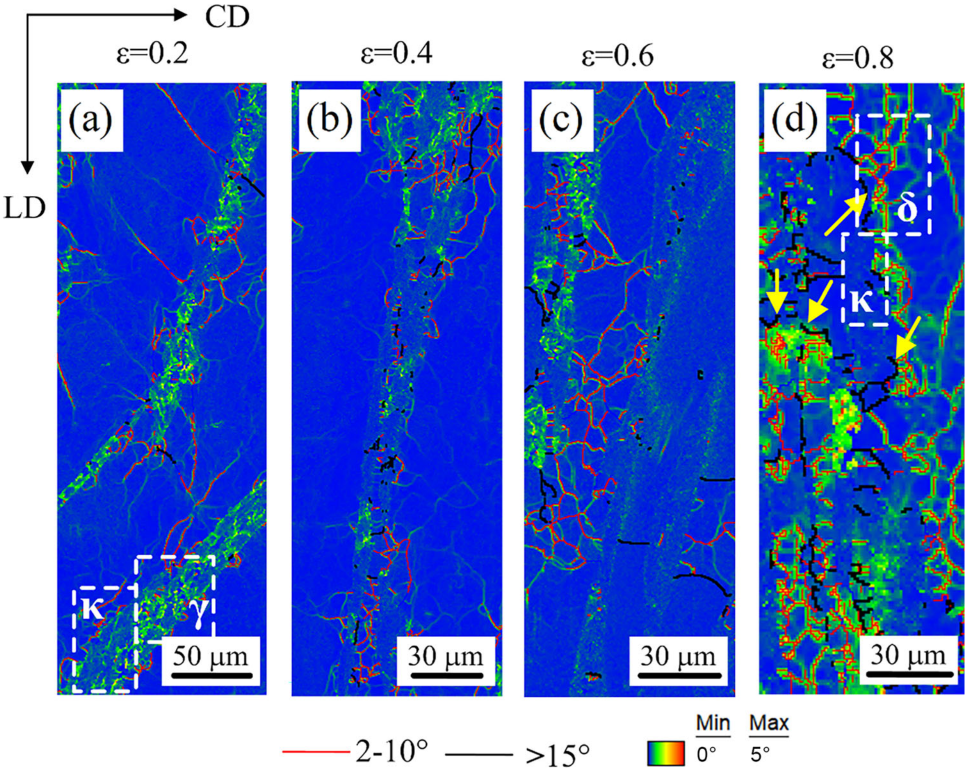

Fig. 18—KAM maps of ferritic-based lightweight steel following deformation at 1000 ºC/10 s^{-1} at different strains: (*a*) 0.2; (*b*) 0.4; (*c*) 0.6; (*d*) 0.8.

steel to effectively distribute strain and adjust to the complex loading conditions encountered during plastic deformation. As depicted in Figure 15, it was apparent that the values of the relative frequency of $\sum 3$ twin boundaries increased as the deformation proceeded. When the applied strain reaches its maximum value of 0.8, the local strain transferred to δ-ferrite adjacent to the lamellar structures (Figure 18(d)). Overall, the behavior of strain localization and its correlation with the microstructural features corroborated well with the fluctuating flow curves observed in Figure 3(d).

V. CONCLUSIONS

In this study, we investigated the hot deformation behavior of a ferritic-based duplex lightweight steel through hot compression tests conducted over a wide range of strain rates (0.01-10 s^{-1}) and temperatures

(800-1100 ºC). The obtained true stress-strain data were utilized to determine the activation energy and establish a processing map. Comprehensive analysis of microstructure evolution and deformation mechanisms was carried out in representative regions corresponding to the processing map. Through the above several aspects of research, the following conclusions can be drawn:

(1) During the initial stages of plastic deformation, an unusual yield point-like phenomenon was evident in the true stress-strain curves of this lightweight steel, which occurred at all strain rates. This phenomenon can be attributed to the combined effects of inhomogeneous strain partitioning within the multiphase containing δ-ferrite, austenite and κ-carbide, along with the presence of high back stress.

(2) As the applied strain continued, the dominant deformation mechanism in specimens exhibiting multiple peaks in flow curves was primarily κ-carbide hardening. This was facilitated by the effective initiation of twinning deformation caused by the augmented occurrence of $\sum 3$ twin boundaries.

(3) With further deformation, the development of substructures bounded by high and low-angle grain boundaries within the δ-ferrite grain promoted continuous dynamic recrystallization. On the contrary, some newly recrystallized grains with high-angle grain boundaries formed at the interface boundaries of δ-ferrite and lamellar structures, representing discontinuous dynamic recrystallization. Both deformation mechanisms are responsible for the multiple valleys observed in the flow curves.

(4) The domain lying in 950-1100 °C/0.01-1 s^{-1} corresponded to the most favorable conditions for hot deformation. The mechanism was influenced by the deformation-induced formation of intra-granular and inter-granular κ-carbides. The former promoted strain hardening, while the latter facilitated dynamic recrystallization.

(5) The unsafe domain at lower temperatures (< 950 °C) and higher strain rates ($> 1\ s^{-1}$) was related to the inhomogeneity in microstructure size and crystallographic orientation.

ACKNOWLEDGMENTS

This work was financially supported by the National Natural Science Foundation of China (General Program No. 52101046).

AUTHOR CONTRIBUTIONS

Wenting Zhu: Data curation, investigation, formal analysis, writing–original draft, conceptualization. Shuangjie Chu: Funding acquisition, supervision, project administration. Bo Mao: Funding acquisition, methodology, writing–review and editing.

DATA AVAILABILITY

Data will be made available on request.

CONFLICT OF INTEREST

The authors declare that they have no known competing financial interests or personal relationships that could have appeared to influence the work reported in this paper.

REFERENCES

1. M.X. Liu, J.Y. Zhou, J.K. Zhang, C.J. Song, and Q.J. Zhai: *Mater. Char.*, 2022, vol. 190, 112042.
2. Z.W. Wang, W.J. Lu, H. Zhao, J.Y. He, K. Wang, B.C. Zhou, D. Ponge, D. Raabe, and Z.M. Li: *Acta Mater.*, 2020, vol. 198, pp. 258–70.
3. A. Zargaran, T.T.T. Trang, G. Park, and N.J. Kim: *Acta Mater.*, 2021, vol. 220, 117349.
4. S. Saberipour, A. Zarei-Hanzaki, H.R. Abedi, and M. Moallemi: *J. Mater. Res. Technol.*, 2022, vol. 18, pp. 755–68.
5. X.Y. Xu, X.M. Wang, J.Z. Li, Z.P. Yan, D. Liu, Q.N. Liu, C.J. Shang, J.X. Fu, and P. Shen: *Mater. Sci. Eng. A*, 2021, vol. 799, 140257.
6. C. Castan, F. Montheillet, and A. Perlade: *Scripta Mater.*, 2013, vol. 68, pp. 360–64.
7. P. Cizek: *Acta Mater.*, 2016, vol. 106, pp. 129–43.
8. B.H. Sun, H. Aydin, F. Fazeli, and S. Yue: *Metall. Mater. Trans. A*, 2016, vol. 47A, pp. 1782–91.
9. D.G. Liu, H. Ding, X. Hu, D. Han, and M.H. Cai: *Mater. Sci. Eng. A*, 2020, vol. 772, 138682.
10. S. Jeong, G. Park, B. Kim, J. Moon, S.-J. Park, and C. Lee: *Mater. Sci. Eng. A*, 2019, vol. 742, pp. 61–68.
11. A. Banis, A. Gomez, V. Bliznuk, A. Dutta, I. Sabirov, and R.H. Petrov: *Mater. Sci. Eng. A*, 2023, vol. 875, 145109.
12. M.N. Elkot, B. Sun, X.Y. Zhou, D. Ponge, and D. Raabe: *Acta Mater.*, 2022, vol. 241, 118392.
13. D.G. Liu, H. Ding, D. Han, and M.H. Cai: *Mater. Sci. Eng. A*, 2022, vol. 833, 142553.
14. S.-W. Park, J.Y. Park, K.M. Cho, J.H. Jang, S.-J. Park, J. Moon, T.-H. Lee, and J.-H. Shin: *Met. Mater. Int.*, 2019, vol. 25, pp. 683–96.
15. C. Haase, C. Zehnder, T. Ingendahl, A. Bikar, F. Tang, B. Hallstedt, W.P. Hu, W. Bleck, and D.A. Molodov: *Acta Mater.*, 2017, vol. 122, pp. 332–43.
16. J. Sun, J.H. Li, P. Wang, and Z.Y. Huang: *Trans. Indian Inst. Met.*, 2022, vol. 75, pp. 699–716.
17. L.X. Xu, H.B. Wu, and B.S. Xie: *Mater. Sci. Technol.*, 2018, vol. 34, pp. 229–41.
18. H.J. McQueen, S. Yue, N.D. Ryan, and E. Fry: *J. Mater. Process. Technol.*, 1995, vol. 53, pp. 293–310.
19. C.M. Sellars and W.J. McTegart: *Acta Mater.*, 1966, vol. 14, pp. 1136–38.
20. H. Mirzadeh, A. Najafizadeh, and M. Moazeny: *Metall. Mater. Trans. A*, 2009, vol. 40, pp. 2950–58.
21. X.Y. Xu, J.Z. Li, W.J. Li, Q.N. Liu, D. Liu, X.M. Wang, J.L. Wang, C.J. Shang, and R.D.K. Misra: *Mater. Des.*, 2019, vol. 180, 107924.

22. Y.P. Li, R.B. Song, E.D. Wen, and F.Q. Yang: *Acta Metall. Sin-Engl.*, 2016, vol. 29, pp. 441–49.
23. P. Rawat, U. Prakash, and V.V. Satya Prasad: *J. Mater. Eng. Perform.*, 2023, vol. 32, pp. 4541–54.
24. A. Mohamadizadeh, A. Zarei-Hanzaki, A. Kisko, and D. Porter: *Mater. Des.*, 2016, vol. 92, pp. 322–29.
25. Y.V.R.K. Prasad, H.L. Gegel, S.M. Doraivelu, J.C. Malas, J.T. Morgan, K.A. Lark, and D.R. Barker: *Metall. Mater. Trans. A*, 1984, vol. 15A, pp. 1883–92.
26. H. Ziegler: *Progress in Solid Mechanics*, 1st ed. North-Holland, Amsterdam, New York, 1963, pp. 93–193.
27. D.W. Kim, S. Lee, and S.S. Sohn: *Scripta Mater.*, 2022, vol. 210, 114477.
28. D. Samantaray, S. Mandal, and A.K. Bhaduri: *Mater. Sci. Eng. A*, 2011, vol. 528, pp. 5204–11.
29. A. Momeni, S.M. Abbasi, and H. Badri: *Appl. Math. Model.*, 2012, vol. 36, pp. 5624–32.
30. E.I. Poliak and J.J. Jonas: *ISIJ Int.*, 2003, vol. 43, pp. 684–91.
31. S.L. Semiatin, D.S. Weaver, R.C. Kramb, P.N. Fagin, M.G. Glavicic, R.L. Goetz, N.D. Frey, and M.M. Antony: *Metall. Mater. Trans. A*, 2004, vol. 35A, pp. 679–93.
32. M.J. Zhao, L. Huang, R. Zeng, H.L. Su, D.X. Wen, and J.J. Li: *Mater. Char.*, 2020, vol. 159, 109997.
33. X. Wang, K. Chandrashekhara, M.F. Buchely, S. Lekakh, D.C. Van Aken, R.J. O'Malley, G.W. Ridenour, and E. Scheid: *J. Manuf. Process.*, 2020, vol. 52, pp. 281–88.
34. Y. Xu, Y.X. Jiao, and J.S. Liu: *J. Mater. Eng. Perform.*, 2020, vol. 29, pp. 4754–65.
35. X.Y. Sun, M. Zhang, Y. Wang, and J. Liu: *Steel Res. Int.*, 2021, vol. 92, p. 2000443.
36. A. Sarkar, S. Sanyal, T.K. Bandyopadhyay, and S. Mandal: *Mater. Char.*, 2017, vol. 134, pp. 213–24.
37. S. Gourdet and F. Montheillet: *Acta Mater.*, 2003, vol. 51, pp. 2685–99.
38. M.F. Ashby: *Philos. Mag. A*, 1966, vol. 14, pp. 1157–78.